batteries

MDPI

Article

Structurally Robust Prussian Blue Nanocubes as High-Rate Cathode Materials for Sodium- and Lithium-Ion Batteries

Narasimharao Kitchamsetti [1,*], Ana L. F. de Barros [2,*], Sungwook Mhin [3,*] and HyukSu Han [4,*]

[1] Department of Microsystems, University of South-Eastern Norway, Campus Vestfold, Raveien 215, 3184 Borre, Norway
[2] Laboratory of Experimental and Applied Physics, Centro Federal de Educação Tecnológica Celso Suckow da Fonseca, Av. Maracanã Campus 229, Rio de Janeiro 20271-110, Brazil
[3] Department of Energy and Materials Engineering, Dongguk University, Seoul 04620, Republic of Korea
[4] Division of Materials Science and Engineering, Hanyang University, Seoul 04763, Republic of Korea
* Correspondence: narasimharao.kitchamsetti@usn.no (N.K.); ana.barros@cefet-rj.br (A.L.F.d.B.); swmhin@dongguk.edu (S.M.); hyuksuhan@hanyang.ac.kr (H.H.)

Abstract

Prussian blue (PB) nanocubes have been explored as promising cathode materials for high-performance sodium-ion (SIBs) and lithium-ion batteries (LIBs). These nanostructures exhibit good cycling stability and electrochemical resilience. They are synthesized through a co-precipitation method followed by vacuum drying, resulting in a porous and conductive nanocube framework. This architecture facilitates efficient ion diffusion, enhanced electrolyte accessibility, and effective mitigation of volume changes during cycling. In SIB applications, the PB nanocubes maintain stable performance over 300 and 400 cycles at current densities of 0.05 and 0.1 A g^{-1}, respectively, and deliver a capacity of 26.2 mAh g^{-1} at 2.0 A g^{-1}. For LIBs, they exhibit sustained cycling over 200 and 300 cycles under similar conditions, with a capacity of 20.2 mAh g^{-1} at 2.0 A g^{-1}. These findings underscore the structural benefits of PB nanocubes for dual-ion battery systems.

Keywords: co-precipitation; prussian blue; cathode; nanocubes; sodium-ion batteries; lithium-ion batteries

1. Introduction

Lithium-ion (LIBs) and sodium-ion batteries (SIBs) are extensively utilized in electric vehicles (EVs), hybrid electric vehicles (HEVs), and portable electronic devices due to their high energy density and prolonged cycling life [1–4]. Among the key components, the cathode material critically determines the overall electrochemical performance of these systems [5,6]. In particular, both the crystal structure and surface characteristics of the cathode strongly influence battery behavior. Therefore, the rational design and selection of cathode materials are essential for achieving high-performance energy storage systems. Common cathode materials for LIBs include $LiCoO_2$ [7], $LiMn_2O_4$ [8], and $LiFePO_4$ [9]. $LiCoO_2$ exhibits favorable cycling stability and good electronic conductivity [10]; however, its practical capacity is significantly lower than its theoretical value, and structural phase transitions during delithiation lead to capacity fading [11]. $LiMn_2O_4$ offers advantages such as low cost, high operating voltage, and environmental compatibility [12], but suffers from Mn dissolution induced by Jahn–Teller distortion, resulting in rapid performance degradation [13]. $LiFePO_4$ provides high theoretical capacity, good stability, and enhanced safety, making it widely used in EVs and HEVs [14]; nonetheless, its low intrinsic conductivity and slow lithium-ion diffusion limit its rate performance [15]. For SIBs, several

Check for updates

Academic Editor: Xianyong Wu

Received: 16 April 2026
Revised: 15 May 2026
Accepted: 16 May 2026
Published: 19 May 2026

Copyright: © 2026 by the authors. Licensee MDPI, Basel, Switzerland. This article is an open access article distributed under the terms and conditions of the Creative Commons Attribution (CC BY) license.

transition-metal oxides, such as $Na_{0.44}MnO_2$ [16], V_2O_5 [17] and $Na_{0.27}Ru_4O_9$ [18], have been investigated, although their reversible capacities are typically limited to relatively low values. Consequently, the development of novel cathode materials with high capacity and durable cycling stability remains a major challenge for next-generation LIBs and SIBs.

Prussian blue (PB) and its analogues have gained significant interest in fields such as adsorption, catalysis, and electrochemical energy storage due to their tunable crystal structures, large surface areas, low cost, and simple synthesis [19–21]. Unlike conventional cathode materials (e.g., metal oxides, phosphates, and fluorides) that often require high-temperature processing, PB compounds can be synthesized from low-cost precursors under mild conditions [22]. Their open framework structures, high Li^+/Na^+ storage capacity, and facile preparation make them promising cathode materials for both LIBs and SIBs [23,24]. PB materials are typically prepared via precipitation or hydrothermal methods, although alternative techniques, including electrodeposition, microemulsion, sonochemical, and microwave-assisted approaches, have also been explored [25]. Despite the diversity of synthesis routes, many methods remain complex and yield limited product quantities, hindering large-scale production [26]. PB compounds commonly contain multiple transition metals in different oxidation states, providing abundant redox-active sites that enable multi-electron transfer at relatively low potentials, thereby enhancing energy storage performance [27]. Notably, PB exhibits a high theoretical capacity (>150 mAh g^{-1}), attributed to dual redox centers [28]. In addition, K^+ ions within the framework enhance Coulombic interactions with nitrogen (N) atoms, leading to lattice expansion that facilitates reversible Li^+/Na^+ insertion and extraction [19–21]. However, challenges such as limited cycling stability and an incomplete understanding of electrochemical mechanisms continue to restrict the broader application of PB-based cathodes.

Inspired by the intrinsic advantages of PB materials and nanocube morphologies, we employ a co-precipitation strategy to synthesize porous PB nanocubes with controlled structure and composition. Rather than introducing a fundamentally new synthesis route, this work focuses on understanding how synthesis conditions influence morphology, composition, and electrochemical behavior. The obtained nanocubes exhibit an interconnected porous framework that facilitates electron transport and provides accessible pathways for ion diffusion, thereby promoting efficient charge transfer and reversible redox reactions during cycling. In addition, the porous architecture improves electrode–electrolyte contact, enhancing wettability and reaction kinetics. Importantly, the as-prepared PB nanocubes are systematically evaluated in both LIBs and SIBs, enabling a direct comparison of their electrochemical behavior across different charge carriers. Through this combined structural and electrochemical analysis, this study provides insights into the structure–composition–performance relationship in PB-based cathodes, demonstrating a balance between practical synthesis, structural stability, and electrochemical functionality.

2. Experimental Section

2.1. Preparation of Prussian Blue Nanocubes

Potassium hexacyanoferrate(III) ($K_3Fe(CN)_6$) and hydrochloric acid (HCl), both of analytical grade, were used without further purification. In a typical procedure, 2 mmol of $K_3Fe(CN)_6$ (99% purity, M.W. 329.24, Sigma-Aldrich) and 1 mL of HCl (37%, M.W. 36.46, Sigma-Aldrich) were dissolved in 100 mL of deionized (DI) water to obtain a homogeneous solution. The mixture was stirred vigorously and heated at 60 °C for 4 h to synthesize PB nanocubes. The product was subsequently collected by centrifugation, washed repeatedly with DI water and ethanol, and dried in a vacuum oven at 90 °C for 24 h.

2.2. Characterization Techniques

The morphology and microstructure of the PB nanocubes were investigated using scanning electron microscopy (SEM, SEM-SU 8000) and transmission electron microscopy (TEM, JEM-2100F). The phase composition and crystal structure were analyzed by X-ray diffraction (XRD) employing Cu Kα radiation on a SmartLab diffractometer. Surface chemical states and electronic structures were examined via X-ray photoelectron spectroscopy (XPS, USWHA150) with a microfocused monochromatic Al Kα source. Raman spectroscopy (JYHR-800, 488 nm excitation) was used to assess the structural ordering of carbon materials. Textural properties, including specific surface area and pore size distribution, were determined from N_2 adsorption–desorption isotherms using the BET method and Barrett–Joyner–Halenda (BJH) model on a Quantachrome analyzer. Thermogravimetric analysis (TGA, Pyris 1, PerkinElmer) was conducted in nitrogen atmosphere from 25 to 800 °C, with a ramping rate of 10 °C min^{-1}. The chemical compositions of the PB compound by ICP calibration of Na and Fe contents and elemental analysis of C and N contents, by which the accurate content of the elements could be determined.

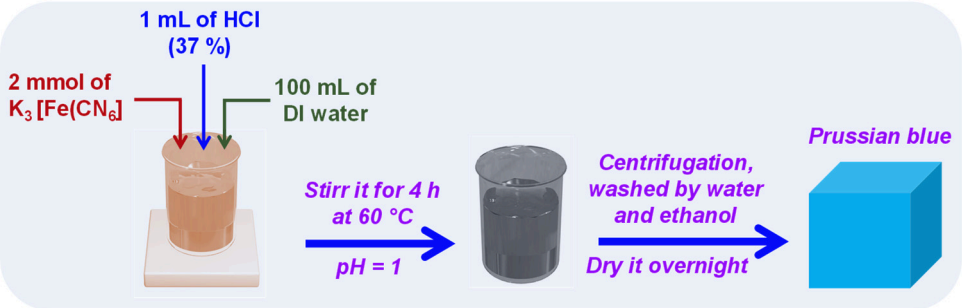
2.3. Electrochemical Measurements

CR2032 coin cells were assembled in an argon-filled glove box at room temperature (22–28 °C) to evaluate the electrochemical performance in both LIB and SIB systems. The working electrodes were fabricated by coating a slurry containing active material, acetylene black, and polyvinylidene fluoride (PVDF) in a mass ratio of 7:2:1 onto aluminum foil, followed by drying at 60 °C overnight. Circular electrodes (14 mm diameter) with an areal loading of ~1 mg cm^{-2} were punched and transferred into the glove box for assembly. For SIBs, sodium metal served as both counter and reference electrodes, with a microporous polypropylene separator (Celgard 2400). The electrolyte consisted of 1.0 M $NaClO_4$ in ethylene carbonate/diethyl carbonate (EC/DEC, 1:1 v/v) with 5% fluoroethylene carbonate (FEC). For LIBs, lithium metal was used as the counter/reference electrode, with Celgard 2400 as the separator and 1.0 M $LiPF_6$ in FEC/dimethyl carbonate (DMC, 1:1 v/v) as the electrolyte. Electrochemical performance was evaluated using cyclic voltammetry (CV), galvanostatic charge–discharge (GCD), and electrochemical impedance spectroscopy (EIS). CV measurements were conducted at 0.1 mV s^{-1}, while GCD tests were performed at current densities ranging from 0.01 to 2.0 A g^{-1} using a Neware battery tester. All measurements were carried out within a voltage range of 2.0–4.2 V. EIS analysis was performed on a CHI 760E workstation over a frequency range of 0.01–100 kHz with an amplitude of 10 mV.

3. Results and Discussion

PB nanocubes were synthesized via a simple co-precipitation method, as illustrated in Scheme 1. Initially, $K_3[Fe(CN)_6]$ was dissolved in DI water under continuous stirring to form a homogeneous precursor solution. Subsequently, concentrated HCl was added dropwise to regulate the acidity of the solution, resulting in a strongly acidic environment (pH ≈ 1). This acidic condition plays a crucial role in controlling both nucleation and crystal growth processes. Specifically, the high proton concentration slows down the coordination reaction between Fe species and $[Fe(CN)_6]^{3-}$ ions, thereby suppressing rapid nucleation and enabling a more controlled formation of nuclei. In addition, the reduced supersaturation under low-pH conditions promotes uniform crystal growth and minimizes particle aggregation, favoring the development of well-defined cubic morphology. The reaction mixture was maintained at 60 °C and stirred for 4 h, during which a dark blue precipitate gradually formed, indicating the formation of PB nanocubes. The controlled growth kinetics under acidic conditions further facilitate the formation of a crystalline Fe-

C≡N-Fe framework with improved structural uniformity. The product was then separated by centrifugation, thoroughly washed with DI water and ethanol to remove residual impurities, and dried overnight to obtain the final PB nanocubes.



Scheme 1. Schematic representation of PB nanocube synthesis via a co-precipitation method.

The morphology and microstructure of the synthesized PB were examined by electron microscopy, as shown in Figure 1a–d. The low-magnification SEM image (Figure 1a) indicates that the particles are uniformly distributed with a narrow size distribution. At higher magnification (Figure 1b), well-defined cubic structures are clearly observed, suggesting that the co-precipitation method enables controlled crystal growth. The nanocubes exhibit lateral dimensions on the order of several hundred nanometers. TEM images (Figure 1c,d) further confirm the formation of uniform cubic particles with sharp edges and smooth surfaces. The SAED pattern (Figure 1e) displays distinct diffraction rings corresponding to the (200), (220), (400), and (420) planes of cubic PB. The measured interplanar spacings of 0.514, 0.364, 0.257, and 0.230 nm agree well with standard values, indicating high crystallinity and phase purity. XRD analysis (Figure 1f) further verifies the crystal structure, with all diffraction peaks indexed to a face-centered cubic PB phase (PDF#73-0687) and no detectable impurities. EDS elemental mapping (Figure 1g) demonstrates the uniform distribution of C, N, K, Fe, and O within the nanocubes, confirming the successful formation of K-containing PB and a well-integrated framework conducive to ion transport.

Raman spectroscopy was used to investigate the local bonding environment and structural integrity of the PB framework (Figure S1). Two distinct peaks located at ~2080 and ~2148 cm^{-1} are observed, corresponding to the characteristic C≡N stretching vibrations of PB-type compounds [22,29]. The sharp and well-defined nature of these bands confirms the successful formation of the cyanide-bridged Fe-C≡N-Fe network. The band near 2080 cm^{-1} is attributed to C≡N stretching associated with Fe^{2+}-C≡N-Fe^{3+} linkages, while the peak at ~2148 cm^{-1} arises from cyanide groups coordinated to a more oxidized Fe environment [22,29]. The presence of both vibrational modes indicates a mixed-valence Fe^{2+}/Fe^{3+} system, a characteristic feature of PB materials that is beneficial for Li^+/Na^+ storage. This mixed valence enhances electronic conductivity and promotes redox activity during ion insertion and extraction.

The thermal stability and chemical composition of the synthesized PB nanocubes were evaluated using thermogravimetric analysis (TG) and X-ray photoelectron spectroscopy (XPS), as shown in Figure 2. To study the chemical formula of the as-obtained PB material, the contents of metal ions and crystal H_2O were analyzed via ICP, TG, and elemental analysis. The TG profile is presented in Figure 2a. It can be divided into three stages: (1) the loss of adsorbed H_2O on the surface of PB material (below 100 °C); (2) loss of crystal water (100–300 °C); (3) PB material decomposition (300–450 °C) [29]. Consequently, the crystal H_2O proportion of the PB material is about 24%. Further gradual weight loss at higher temperatures indicates continued structural degradation. The ICP and elemental analysis test results (Table S1) of as-obtained PB material shows that the weight percentages of Fe,

K, C, and N elements are about 34.5%, 6.1%, 20.5% and 23.7%, respectively. Based on the elemental analysis and ICP result and TG test, the chemical formula of the as-prepared PB should be $K_{1.06}Fe[Fe(CN)_6]\cdot 2.8H_2O$. The XPS survey spectrum (Figure 2b) verifies the presence of Fe, C, N, K, and O elements, consistent with K-containing PB, and no impurity signals are detected, indicating high chemical purity [30,31]. The high-resolution Fe 2p spectrum (Figure 2c) exhibits two distinct spin–orbit doublets assigned to Fe^{2+} and Fe^{3+} species. Peaks located at 709.7 and 723.6 eV correspond to Fe^{3+} (Fe $2p_{3/2}$ and Fe $2p_{1/2}$), while those at 712.2 and 725.5 eV are attributed to Fe^{2+}, along with their associated satellite features, confirming a mixed-valence state [20,32]. The K 2p and C 1s spectra (Figure 2d) show characteristic K $2p_{3/2}$ and K $2p_{1/2}$ peaks, indicating successful incorporation of K ions into the PB framework. The C 1s spectrum can be deconvoluted into components corresponding to C≡N/C-C (285.4 eV), C=C (~284.1 eV), and C-O (288.4 eV), reflecting the cyanide coordination and slight surface oxidation [4,33]. The N 1s spectrum (Figure 2e) includes pyridinic N (398.2 eV), pyrrolic N (400.1 eV), graphitic N (402.5 eV), and oxidized N (405.7 eV) species, confirming the presence of nitrogen functionalities derived from cyanide ligands [34,35]. Furthermore, the O 1s spectrum (Figure 2f) reveals contributions from Fe-O (528.6 eV), C=O/C-O (529.8 eV), and hydroxyl groups (C-OH, 530.8 eV), which can be attributed to coordinated water molecules and surface oxidation [36,37]. These oxygen-containing species may enhance electrolyte wettability and facilitate ion transport.

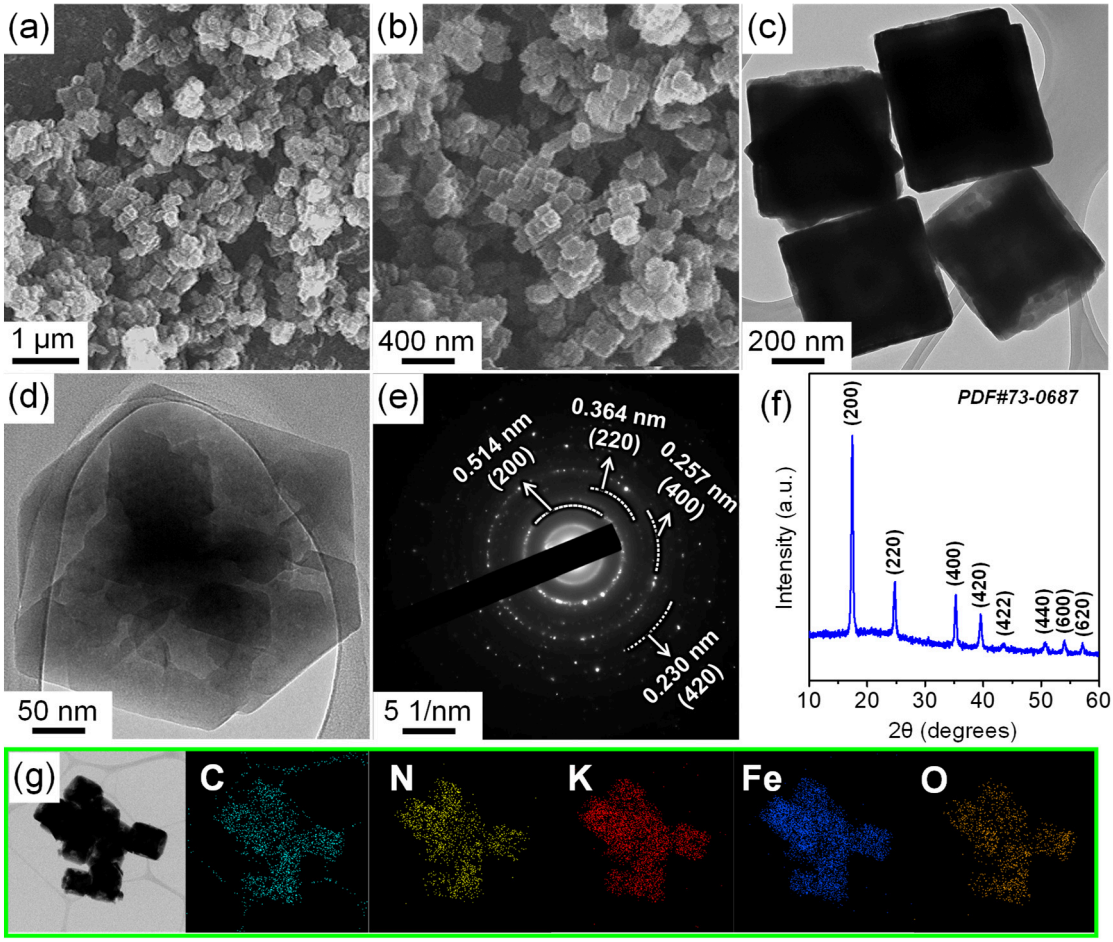


Figure 1. Morphologies, XRD pattern, and elemental mapping images of the PB nanocubes obtained after the co-precipitation followed by vacuum drying: (**a**,**b**) FE-SEM images, (**c**,**d**) TEM images, (**e**) SAED pattern, (**f**) XRD pattern, and (**g**) elemental mapping images.

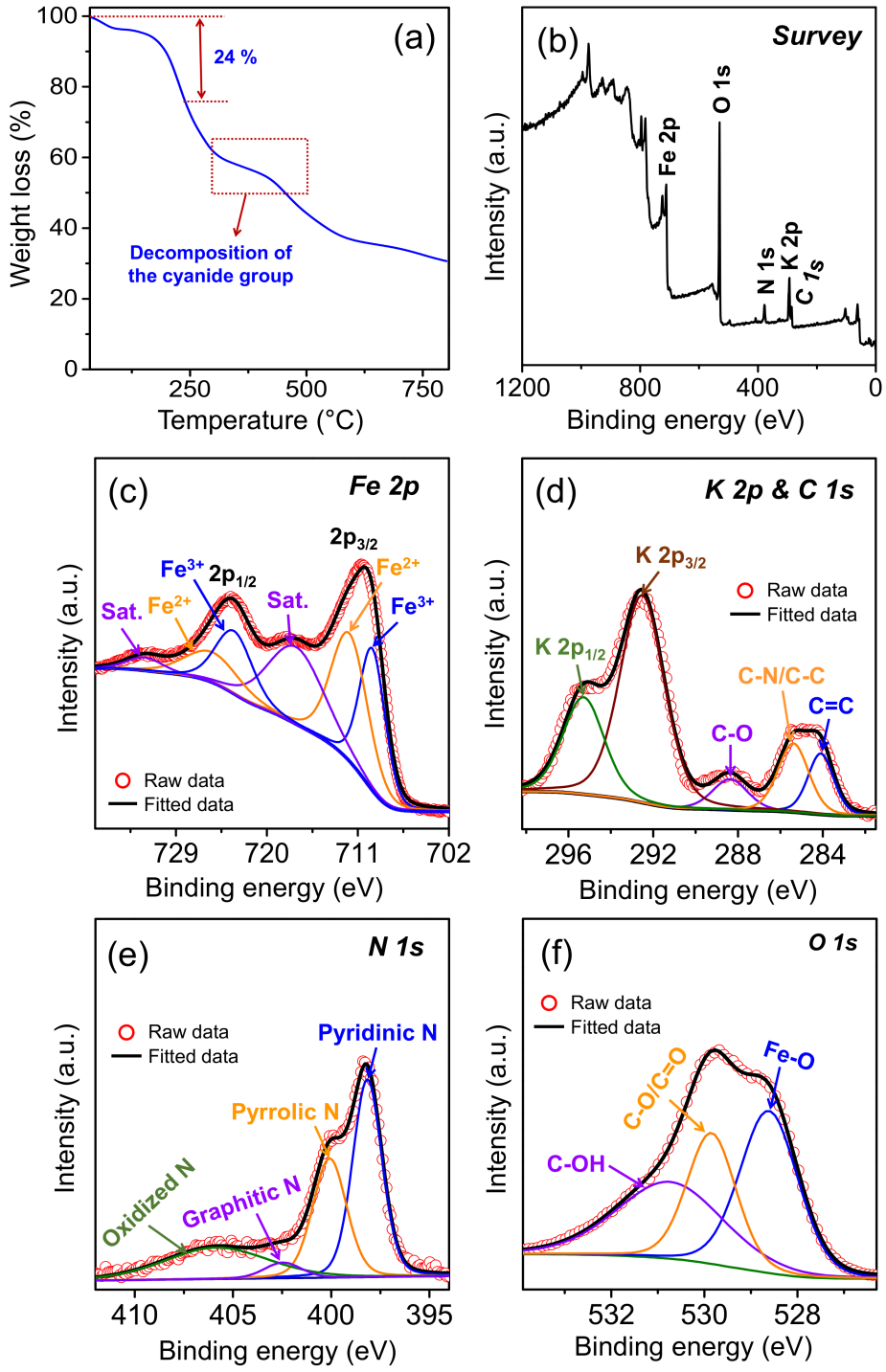


Figure 2. (**a**) TG analysis. (**b**–**f**) XPS survey spectrum, and core level XPS spectra of PB nanocubes: (**b**) XPS survey spectrum, (**c**) Fe 2p, (**d**) K 2p & C 1s, (**e**) N 1s, and (**f**) O 1s.

The textural properties of the PB nanocubes were evaluated by nitrogen adsorption–desorption measurements (Figure S2). The isotherm (Figure S2a) exhibits a typical type-IV profile with a significant uptake at high relative pressures ($P/P_0 > 0.8$), indicative of mesoporous characteristics. The gradual adsorption at low pressures reflects the presence of accessible surface sites, while the sharp increase at higher pressures is attributed to capillary condensation within mesopores formed by the assembly of nanocubes. BET analysis yields a specific surface area of 49.1 $m^2\ g^{-1}$, suggesting a moderately high surface area for PB-based cathodes prepared via co-precipitation. This surface area provides abundant active sites and enhances electrode–electrolyte interaction. The BJH pore size

distribution (Figure S2b) shows a dominant mesoporous structure with an average pore diameter of ~14.7 nm. The broad distribution indicates the coexistence of interparticle voids and intrinsic framework porosity, which facilitates electrolyte infiltration and promotes rapid Li^+/Na^+ diffusion, particularly beneficial for accommodating Na^+ ions during high-rate cycling.

The electrochemical performance of the porous PB nanocubes as LIB cathodes is presented in Figure 3. The CV curves for the first five cycles (Figure 3a), recorded at a scan rate of 0.1 mV s^{-1} within a voltage window of 2.0–4.2 V, display two distinct redox peaks at approximately 2.92 and 3.12 V. These peaks correspond to the reversible Fe^{3+}/Fe^{2+} redox reactions associated with Li^+ insertion and extraction within the cyanide-bridged framework. The strong overlap of the CV profiles from the second to fifth cycles indicates good reversibility and structural stability during repeated cycling. The galvanostatic charge–discharge (GCD) curves in Figure 3b further validate the characteristic electrochemical behavior of PB. Clear voltage plateaus at approximately 3.1 V are observed during both charging and discharging, consistent with the CV analysis. The strong overlap of the profiles in the initial three cycles indicates low polarization and favorable reaction kinetics. The rate capability of the PB nanocube cathode was assessed over a current density range of 0.01–2.0 A g^{-1} (Figure 3c,d). The electrode delivers a high specific capacity of ~86.1 mAh g^{-1} at 0.01 A g^{-1} and retains 20.2 mAh g^{-1} at 2.0 A g^{-1}. When the current density is reduced back to 0.03 A g^{-1}, the capacity is largely recovered, indicating strong structural stability and rapid kinetics. This enhanced rate performance is attributed to the open PB framework, together with the mesoporous structure and nanocube morphology, which shorten Li^+ diffusion pathways and facilitate efficient charge transport. Long-term cycling performance was evaluated at current densities of 0.05 A g^{-1} (Figure 3e) and 0.1 A g^{-1} (Figure 3f). At 0.05 A g^{-1}, the PB cathode retains a reversible capacity of 59.6 mAh g^{-1} after 200 cycles, with coulombic efficiency approaching 100% throughout the test. At a higher current density of 0.1 A g^{-1}, stable cycling is maintained over 300 cycles with only gradual capacity fading, indicating robust structural integrity during repeated Li^+ insertion/extraction.

Likewise, Figure 4a presents the CV profiles of the PB nanocube cathode in Na-ion cells over a voltage window of 2.0–4.2 V (vs. Na^+/Na). As observed in LIBs, clear redox peaks appear at approximately 2.78 and 3.1 V, which are associated with the Fe^{3+}/Fe^{2+} redox couple during Na^+ insertion and extraction. The peaks are slightly broader than those in the lithium system, likely due to the larger ionic radius of Na^+, leading to increased polarization. Figure 4b presents the GCD curves, which exhibit distinct voltage plateaus centered at approximately 3.1 V, indicative of the characteristic redox behavior of PB in SIBs. The strong overlap between consecutive cycles suggests good reversibility of Na^+ insertion/extraction within the PB nanocube framework. As illustrated in Figure 4c,d, the PB cathode demonstrates stable rate capability across a broad current density range (0.01–2.0 A g^{-1}). A reversible capacity of 92.2 mAh g^{-1} is delivered at low current density, while 26.2 mAh g^{-1} is maintained at 2.0 A g^{-1}. Notably, the capacity recovers when the current density is reduced, reflecting robust structural stability and favorable Na^+ diffusion kinetics despite the larger ionic radius. Figure 4e,f present the long-term cycling performance at current densities of 0.05 and 0.1 A g^{-1}, respectively. The PB nanocube cathode maintains stable capacities of 60.4 mAh g^{-1} after 300 cycles at 0.05 A g^{-1} and 54.8 mAh g^{-1} after 400 cycles at 0.1 A g^{-1}. The coulombic efficiency remains close to 100% throughout cycling, indicating highly reversible Na^+ insertion/extraction with negligible side reactions. The similar electrochemical responses observed in both Li- and Na-ion systems demonstrate the structural adaptability of PB nanocubes. Their mixed-valence Fe^{2+}/Fe^{3+} redox chemistry, open framework, and mesoporous architecture collectively

promote efficient alkali-ion transport, good reversibility, and prolonged cycling stability, highlighting their potential as cathode materials for both LIBs and SIBs. Additionally, the electrochemical performance of PB nanocubes prepared in this study is compared with other previously reported PB cathodes in Table S2.

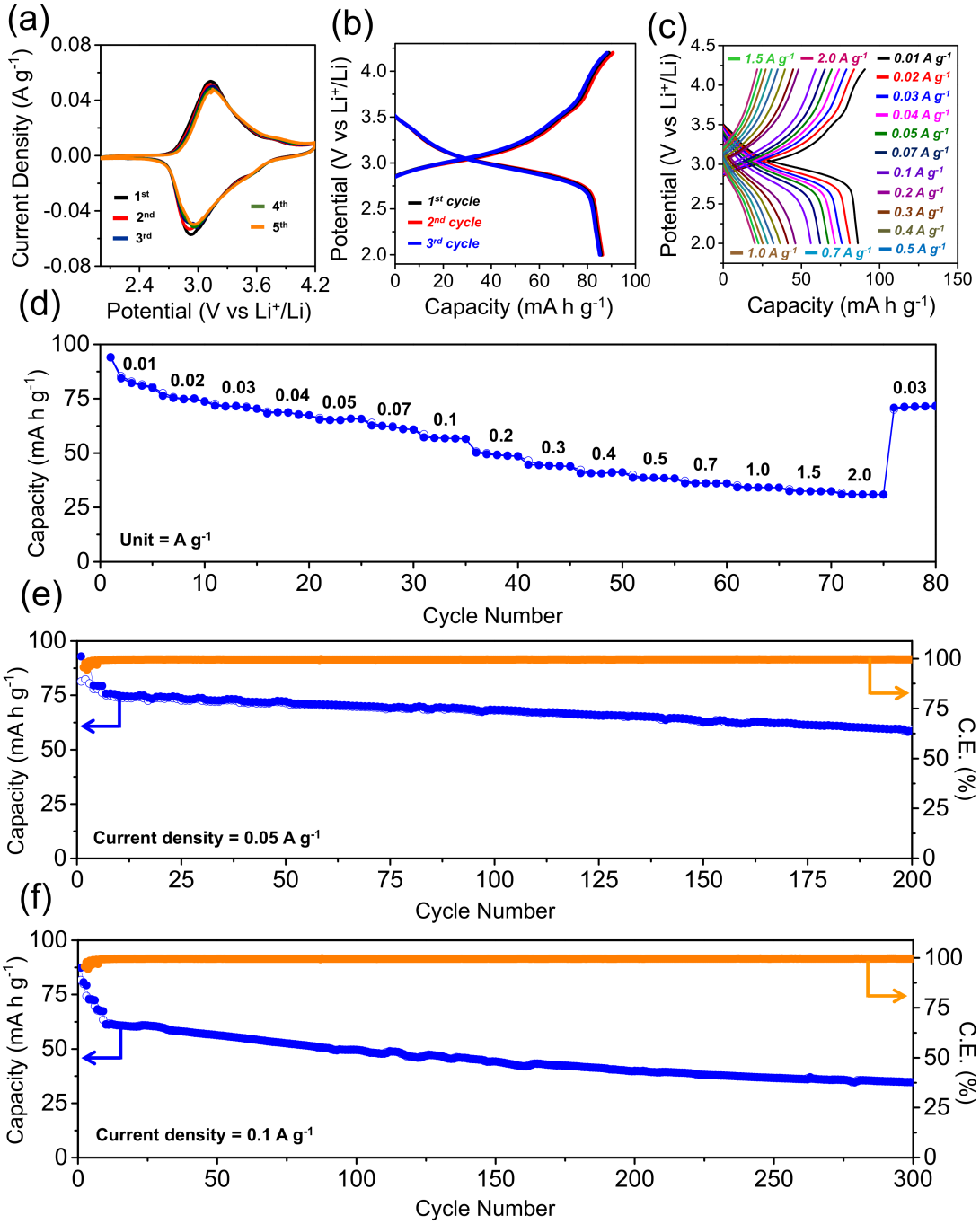


Figure 3. Electrochemical performance of PB nanocubes for Li^+ storage: (**a**) CV plots recorded at a scan rate of 0.1 mV s^{-1}, (**b**) galvanostatic charge–discharge profiles for the first three cycles at 0.01 A g^{-1}, (**c**) charge–discharge plots measured under different current densities, (**d**) rate capability, and cycling performance evaluated at current densities of (**e**) 0.05 A g^{-1} and (**f**) 0.1 A g^{-1}.

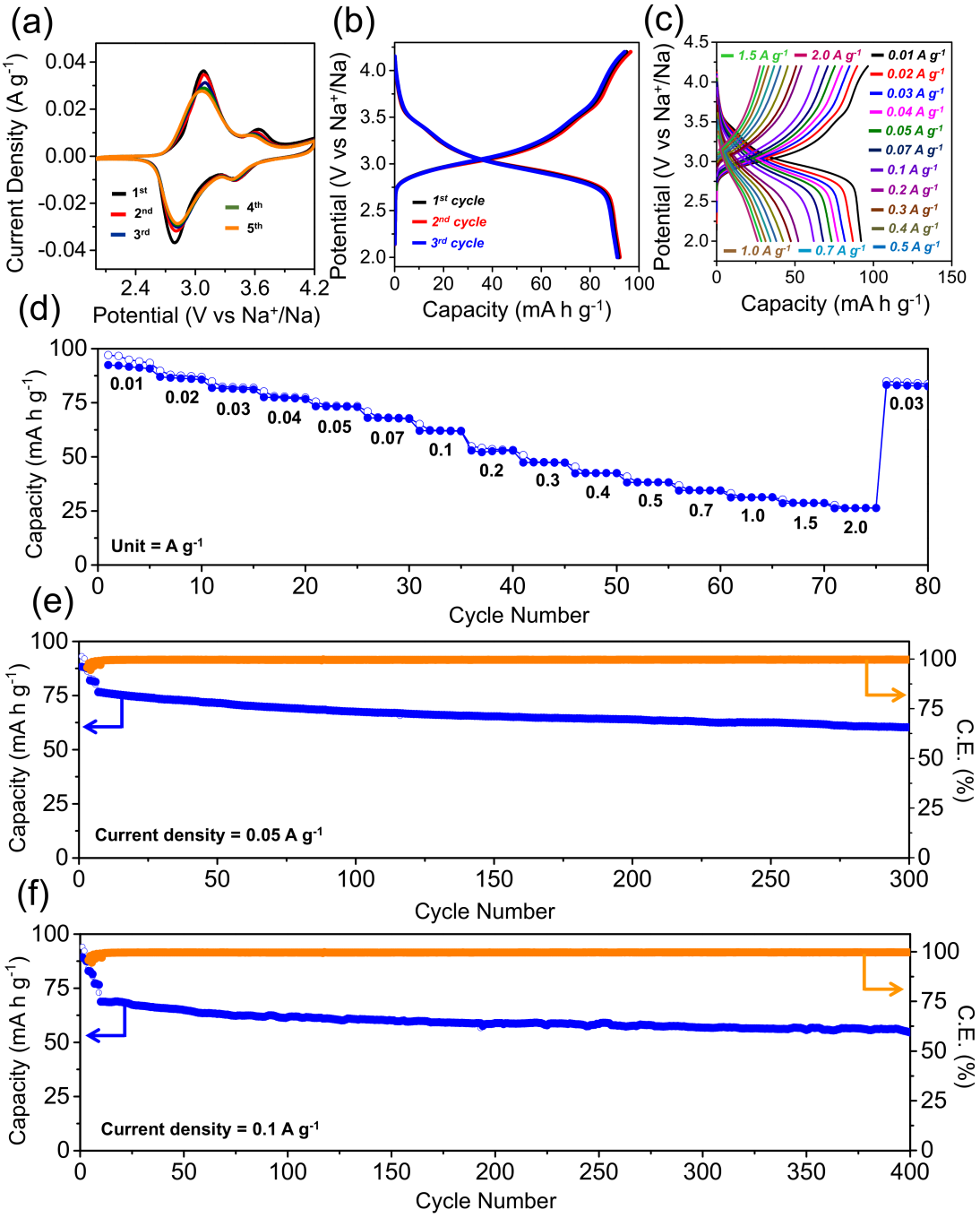


Figure 4. Electrochemical performance of PB nanocubes for Na^+ storage: (**a**) CV plots recorded at a scan rate of 0.1 mV s^{-1}, (**b**) galvanostatic charge–discharge profiles for the initial three cycles at 0.01 A g^{-1}, (**c**) charge–discharge curves measured at various current densities, (**d**) rate capability, and cycling stability evaluated at current densities of (**e**) 0.05 A g^{-1} and (**f**) 0.1 A g^{-1}.

To obtain a deeper understanding of the electrochemical behavior of PB nanocubes in SIBs, CV measurements were performed. Figure 5a presents the CV profiles recorded at scan rates from 0.1 to 1.6 mV s^{-1} over a voltage range of 2.0–4.2 V (vs. Na^+/Na). Two well-defined redox pairs, labeled Peak 1 and Peak 2, correspond to the reversible Fe^{3+}/Fe^{2+} redox reactions associated with Na^+ insertion/extraction processes. As the scan rate increases, the anodic and cathodic peak currents increase correspondingly while the overall peak shapes remain nearly unchanged, indicating favorable reversibility and fast charge-transfer kinetics. Slight shifts in peak potentials at elevated scan rates can be attributed to polarization caused by limitations in Na^+ diffusion, a phenomenon frequently

observed in PB-based cathode materials. To further investigate the sodium-storage behavior, the relationship between peak current (i) and scan rate (ν) was analyzed according to the power–law relationship [38]:

$$i = a\nu^b \quad (1)$$

$$\log(i) = \log(a) + b\log(\nu) \quad (2)$$

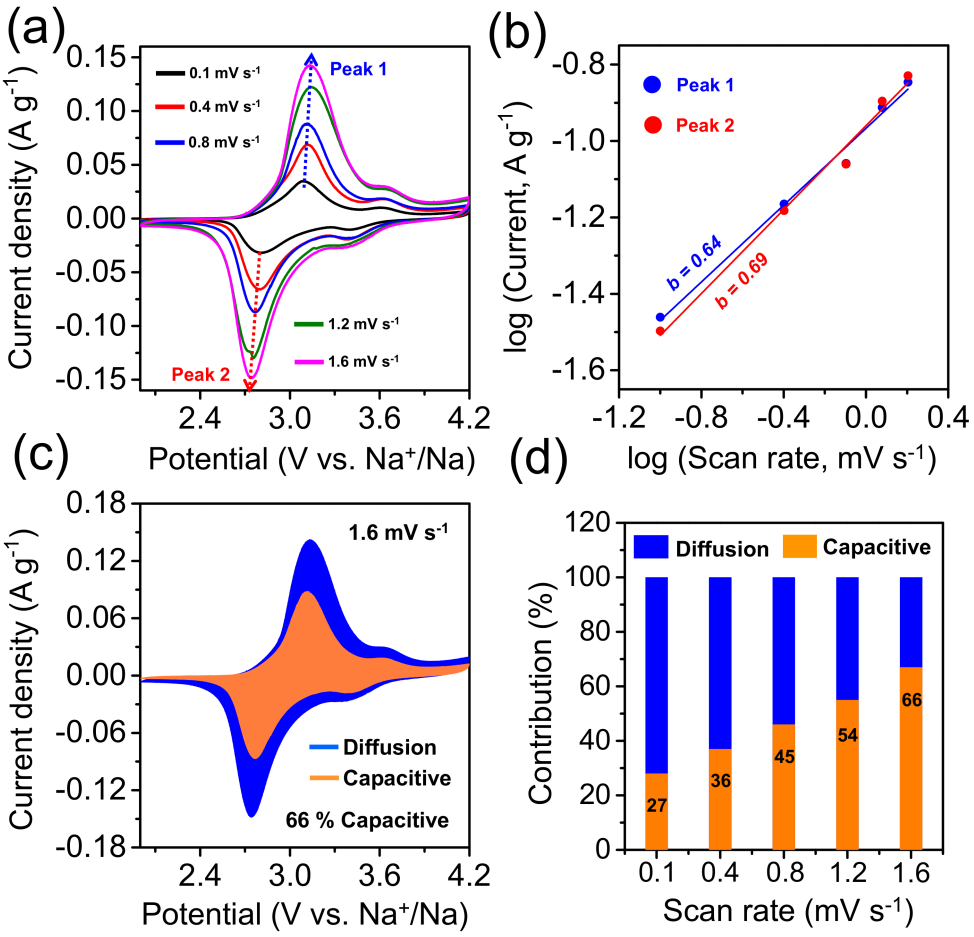


Figure 5. Electrochemical kinetic analysis of PB nanocubes for Na^+ storage: (**a**) CV profiles measured at different scan rates, (**b**) relationship between peak current (i) and scan rate (ν) for each redox peak, (**c**) capacitive contribution highlighted in orange at a scan rate of 1.6 mV s^{-1}, and (**d**) percentage of capacitive contribution at various scan rates.

In this model, the b value is used to identify the dominant charge-storage mechanism. A b value near 0.5 signifies a diffusion-controlled process, whereas a value close to 1.0 indicates surface-controlled capacitive behavior [39]. The b values were obtained from the slopes of the linear relationships between log(i) and log(ν) for both anodic and cathodic peaks, as shown in Figure 5b. The calculated values of approximately 0.64 for Peak 1 and 0.69 for Peak 2 indicate that Na^+ storage in PB nanocubes is mainly governed by capacitive-controlled kinetics. To further separate the individual contributions, the capacitive and diffusion-controlled currents were analyzed using the following equation [40]:

$$i = k_1\nu + k_2\nu^{1/2} \quad (3)$$

where $k_1\nu$ and $k_2\nu^{1/2}$ correspond to the capacitive and diffusion-controlled contributions, respectively, and k_1 and k_2 are constants determined from the slope and intercept of the $i(V)/\nu^{1/2}$ versus $\nu^{1/2}$ plot [41]. As illustrated in Figure 5c, the capacitive contribution accounts for nearly 66% of the total current at a scan rate of 1.6 mV s^{-1}. Moreover,

Figure 5d demonstrates that capacitive behavior dominates across the entire scan-rate range. These results reveal fast Na^+ transport kinetics in the PB nanocube cathode, which may originate from enhanced electrolyte penetration within the porous structure and effective accommodation of volume changes during cycling, thereby promoting efficient charge-transfer reactions.

In addition to the Na^+ system, the electrochemical kinetics of the PB nanocube cathode were also investigated in Li^+ ion cells to enable a direct comparison between the two alkali-ion charge carriers. Figure S3a displays the CV curves recorded at scan rates ranging from 0.1 to 1.6 mV s^{-1} within a voltage window of 2.0–4.2 V (vs. Li^+/Li). Similar to the Na^+ system, two distinct redox couples (Peak 1 and Peak 2) are observed, corresponding to the reversible Fe^{3+}/Fe^{2+} redox reactions during Li^+ insertion/extraction. As the scan rate increases, both anodic and cathodic peak currents increase proportionally while maintaining comparable peak profiles, indicating excellent electrochemical reversibility and rapid reaction kinetics. Minor shifts in peak potentials at higher scan rates are attributed to polarization effects caused by Li^+ diffusion limitations, which are commonly observed in PB-based cathodes. To further clarify the Li^+ storage mechanism, the relationship between peak current (i) and scan rate (ν) was evaluated using the power–law model. The b values obtained from the slopes of the log(i) versus log(ν) plots shown in Figure S3b are approximately 0.71 for Peak 1 and 0.75 for Peak 2, suggesting that the charge-storage process is predominantly governed by capacitive-controlled kinetics. The relative contributions from capacitive and diffusion-controlled processes were further quantified using Equation (3). As illustrated in Figure S3c, the capacitive contribution reaches approximately 71% at a scan rate of 1.6 mV s^{-1} and remains dominant throughout the entire scan-rate range, as summarized in Figure S3d. These results indicate rapid Li^+ transport kinetics in the PB nanocube cathode, which can be attributed to the porous nanocube architecture that promotes electrolyte accessibility and effectively accommodates structural volume variations during repeated cycling.

Electrochemical impedance spectroscopy (EIS) was conducted to further assess the Na^+ transport kinetics and interfacial stability of the PB nanocube cathode. As illustrated in Figure 6, Nyquist plots were recorded for the electrode in the fully charged state both before cycling and after 400 charge–discharge cycles. The impedance data were fitted using a Randles-type equivalent circuit (Figure S4), and the corresponding parameters are summarized in Table S3. For the pristine electrode (Figure 6a,b), the electrolyte resistance (R_s) was approximately 21 Ω, while the charge-transfer resistance (R_{ct}) was about 207 Ω. After 400 cycles, the R_{ct} value significantly decreased to 27 Ω, indicating markedly improved charge-transfer kinetics and enhanced interfacial stability during long-term cycling.

To better understand Na^+ diffusion, the real impedance component (Z_{re}) was plotted against $\omega^{-1/2}$ ($\omega = 2\pi f$) in the low-frequency region (Figure 6c). The PB nanocube cathode shows a relatively small slope, indicating improved Na^+ diffusivity within the electrode. This observation aligns with the electrochemical results, confirming the advantageous diffusion properties of the nanocube structure. The Na^+ diffusion coefficient (D_{Na^+}), calculated from the Warburg region using Equation (4), was found to be 1.1×10^{-9}, $cm^2\ s^{-1}$ [42], suggesting fast ion transport and efficient redox reactions during cycling.

$$D_{Na^+} = \frac{0.5\ R^2\ T^2}{A^2\ F^4\ C^2\ \sigma_W^2} \quad (4)$$

where D_{Na^+} is Na^+-ion diffusion coefficient, R is the gas constant, T is the temperature, A is the electrode area, C is the Na-ion concentration, F is the Faraday constant, and σ_W is the Warburg impedance factor.

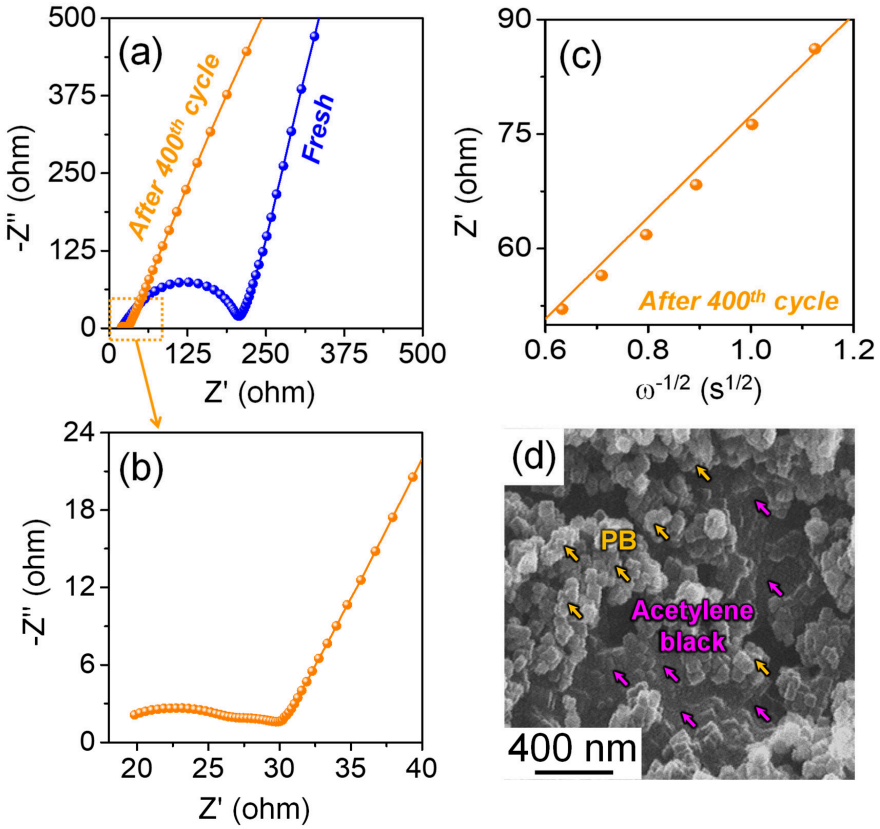


Figure 6. Electrochemical impedance and structural characterization of PB nanocubes after cycling: (**a**,**b**) Nyquist plots measured after 400 cycles at a current density of 0.1 A g^{-1}, (**c**) linear relationship between the real impedance component (Z_{re}) and $\omega^{-1/2}$ after cycling, and (**d**) FE-SEM image of the PB nanocubes following 400 charge/discharge cycles at 0.1 A g^{-1}.

The structural integrity of the electrode after prolonged cycling was further examined by SEM analysis. As shown in Figure 6d, the electrode morphology after 400 cycles at a current density of 0.1 A g^{-1} remains intact, with PB nanocubes uniformly dispersed and tightly integrated with the conductive carbon additive (acetylene black). No obvious particle fracture or structural degradation is observed, corroborating the reduced R_{ct} and stable impedance behavior. This robust electrode architecture effectively preserves electronic conductivity and suppresses impedance growth during repeated Na^+ insertion and extraction.

4. Conclusions

This study reports the successful synthesis of PB nanocubes through a straightforward co-precipitation method followed by vacuum drying. The obtained porous nanocube structure offers ample internal space to buffer volume changes during cycling, while facilitating electrolyte penetration and rapid charge carrier transport. In addition, the interconnected network of PB nanocubes forms continuous conductive pathways, promoting efficient charge transfer and enhanced redox kinetics. As a result, the material exhibits remarkable mechanical robustness and good rate capability when used as a cathode in both SIBs and LIBs. Notably, high discharge capacities are maintained even at a current density of 2 A g^{-1}, highlighting the suitability of this architecture for fast-charging applications. Overall, this structural design provides a promising strategy for developing highly conductive and porous nanomaterials for durable energy storage systems.

Supplementary Materials: The following supporting information can be downloaded at: https://www.mdpi.com/article/10.3390/batteries12050178/s1.

Author Contributions: Conceptualization, N.K.; formal analysis, N.K.; investigation, N.K.; resources, H.H., S.M. and A.L.F.d.B.; data curation, N.K., H.H., S.M. and A.L.F.d.B.; writing—original draft preparation, N.K.; writing—review and editing, N.K., H.H., S.M. and A.L.F.d.B.; visualization, N.K.; supervision, N.K., H.H., S.M. and A.L.F.d.B.; project administration, H.H., S.M. and A.L.F.d.B.; funding acquisition, H.H., S.M. and A.L.F.d.B. All authors have read and agreed to the published version of the manuscript.

Funding: This research was supported by the Nano and Material Technology Development Program through the National Research Foundation (NRF) of Korea funded by the Ministry of Science and ICT (RS-2024-00449682). The authors acknowledge the financial support from the National Research Foundation of Korea (NRF) funded by the Ministry of Science and ICT (RS-2024-00433118). This research was supported by the National Research Foundation (NRF) of Korea, funded by the Government of Korea (MSIT) (RS-2023-00236572).

Institutional Review Board Statement: Not applicable.

Informed Consent Statement: Not applicable.

Data Availability Statement: The original contributions presented in the study are included in the article, further inquiries can be directed to the corresponding authors.

Conflicts of Interest: The authors declare that they have no known competing financial interests or personal relationships that could have appeared to influence the work reported in this paper.

References

1. Liu, M.W.; Li, A.; Lin, H.A.; Li, Z.J.; Wang, L.; Deng, Y.R.; Wang, Y.F.; Liu, R.P.; He, X. Architectural engineering of metal-organic frameworks in lithium-ion batteries: Multifunctional roles, challenges, and future perspectives. *Nano Energy* **2025**, *143*, 111310. [CrossRef]
2. Saghafizadeh, M.A.; Zardkhoshoui, A.M.; Davarani, S.S.H. Hybrid supercapacitors with MnTe@ZnMnTe hollow octahedrons encapsulated with reduced graphene oxide for high-performance hybrid supercapacitors. *Chem. Eng. J.* **2025**, *508*, 160817. [CrossRef]
3. Chen, Z.; Gao, W.; Yang, J.; Wu, Y.; Zhu, M.; He, J. Insight into preparation strategies of biomass-derived hard carbon anodes for sodium-ion batteries. *Chem. Eng. J.* **2025**, *518*, 164774. [CrossRef]
4. Bugday, N.; Deng, W.; Zou, G.; Hou, H.; Ji, X.; Yaşar, S. Cu@MOF based composite materials: High performance anode electrodes for lithium-ion and sodium-ion batteries. *J. Energy Storage* **2024**, *104*, 114570. [CrossRef]
5. Xiao, Y.; Xiao, J.; Zhao, H.; Li, J.; Zhang, G.; Zhang, D.; Guo, X.; Gao, H.; Wang, Y.; Chen, J.; et al. Prussian Blue Analogues for Sodium-Ion Battery Cathodes: A Review of Mechanistic Insights, Current Challenges, and Future Pathways. *Small* **2024**, *20*, 2401957. [CrossRef]
6. Tan, X.; Dong, X.; Zhang, F.; Huang, C.; Zhang, Y. Structure engineering of nickel silicate/carbon composite with boosted electrochemical performances for hybrid supercapacitors. *J. Colloid Interface Sci.* **2024**, *674*, 67–78. [CrossRef]
7. Dou, Y.; Liu, Y.; Chang, Q.; Feng, X.; Xiang, H. Liquid-phase assisted ions gradient doping-coating integration for enhanced high-voltage $LiCoO_2$ performance. *J. Energy Storage* **2026**, *149*, 120334. [CrossRef]
8. Li, J.; Yang, X.; Chen, J.; Yan, G.; Wang, B.; Qin, R.; Li, C.; Su, Y.; Liu, Z.; Parreira, L.S.; et al. Understanding the Role of Nb Doping in Modulating Ionic Diffusion Kinetics and Particle Size in Spinel $LiMn_2O_4$. *Battery Energy* **2026**, *5*, e70074. [CrossRef]
9. Theodore, A.M. Structural, electrical, and electrochemical studies of the olivine $LiMPO_4$ (M = Fe, Co, Cr, Mn, V) as cathode materials for lithium-ion rechargeable batteries based on the intercalation principle. *Mater. Open Res.* **2023**, *2*, 11. [CrossRef]
10. Liu, G.X.; Nie, Q.; Wan, W.; Yang, F.Z.; Yang, Z.; Qu, G.; Guo, L.; Chen, J.; Wei, X.Z.; Huang, Y.; et al. Flash upcycling of spent $LiCoO_2$ into oxygen-suppressed lithium-replenishing agent for high-performance batteries. *Nat. Commun.* **2026**, *17*, 41. [CrossRef]
11. Yu, B.; Yuan, C.; Xu, L.; Zhao, G.; Zheng, Y.; Li, J. Sc_2O_3 coating and Sc gradient doping synergistically enhance high-voltage performance of $LiCoO_2$. *J. Energy Storage* **2026**, *146*, 120071. [CrossRef]
12. Jin, L.; Du, G.; Liu, P.; Gu, T.; Gao, R.; Abdelkader, A.M.; Hua, W.; Xu, M.; Peng, L.; Qiu, B.; et al. Voltage Decay and Capacity Loss in Lithium-Rich Manganese Oxide Cathodes: Atomic Origins, Mesoscopic Heterogeneities, and Macroscopic Evolution. *Adv. Mater.* **2026**, *38*, e21529. [CrossRef]

13. Siddanth, S.G.; Vadnala, S.; Ramesh, A.; Nayak, R. Surface evolution mechanisms and stabilization approaches for lithium manganese oxide in rechargeable Li-ion batteries. *Energy Rep.* **2025**, *14*, 5828–5852. [CrossRef]
14. Wang, T.; Yu, W.; Chen, G.; Gao, C.C.; Zhang, J.; Lin, Y.; Wang, M.; Xu, J.; Yang, C.; Zhang, J. Lactic acid-ethylene glycol system driven materials stripping for efficient and eco-friendly recycling of spent $LiFePO_4$ cathode materials. *J. Mater. Sci. Technol.* **2026**, *250*, 98–107. [CrossRef]
15. Cheng, C.; Cao, X.; Xing, Z.; Tang, S.C. Direct regeneration of severely damaged spent $LiFePO_4$ cathodes. *J. Mater. Sci. Technol.* **2026**, *241*, 262–269. [CrossRef]
16. Liu, Z.M.; Feng, X.T.; Zhao, H.J.; Han, X.Q.; Ye, Z.X.; Yao, Z.C.; Zhang, D. High-Performance B-Doped $Na_{0.44}MnO_2$ Cathode Materials for Sodium-Ion Batteries. *ACS Omega* **2025**, *10*, 10023–10033. [CrossRef]
17. Ba, Y.; Yang, G.; Jiang, R.; Tang, J.; Xu, Y.C.; Liu, W. V_2O_5/Mesocarbon Microbeads Composites with Oxygen Vacancies as Cathodes for Sodium-Ion Batteries. *Energy Fuels* **2026**, *40*, 1778–1785. [CrossRef]
18. Jung, Y.H.; Hong, S.T.; Kim, D.K. Electrochemical Sodium Ion Intercalation Properties of $Na_{2.7}Ru_4O_9$ in Nonaqueous and Aqueous Electrolytes. *J. Electrochem. Soc.* **2013**, *160*, A897–A900. [CrossRef]
19. Chen, Y.H.; Kubendhiran, S.; Lin, C.H.; Lin, L.Y.; Ho, K.C. Two-dimensional molybdenum carbide integrated cobalt iron phosphorus trisulfides derived from Prussian blue analogues for bifunctional electrocatalysis. *J. Power Sources* **2026**, *668*, 239354. [CrossRef]
20. Feng, J.; Luo, S.H.; Lin, Y.C.; Zhan, Y.; Yan, S.X.; Hou, P.Q.; Wang, Q.; Zhang, Y.H. Metal-organic framework derived $CoSe_2$/N-doped carbon core-shell nanoparticles encapsulated in porous N-doped carbon nanotubes as high-performance anodes for sodium-ion batteries. *J. Power Sources* **2022**, *535*, 231444. [CrossRef]
21. Fan, L.; Guo, X.; Li, W.; Hang, X.; Pang, H. Rational design of Prussian blue analogue-derived manganese-iron oxides-based hybrids as high-performance Li-ion-battery anodes. *Chin. Chem. Lett.* **2023**, *34*, 107447. [CrossRef]
22. Fu, W.W.; Wang, D.; Zhang, K.; Zheng, J.; Zhang, M.; Shen, Z. Nanoporous Iron-Based Prussian Blue Analogues for High-Performance Sodium-Ion Batteries. *ACS Appl. Nano Mater.* **2026**, *9*, 1608–1619. [CrossRef]
23. Kitchamsetti, N. A review on recent advances in Prussian blue, its analogues, and their derived materials as electrodes for high performance supercapacitors. *J. Energy Storage* **2023**, *73*, 108958. [CrossRef]
24. Kitchamsetti, N.; de Barros, A.L.F.; Han, H.; Mhin, S. Shaping the future of energy storage with single-atom materials. *J. Alloy Compd.* **2025**, *1044*, 184389. [CrossRef]
25. Iyyappan, M.; Senthil, C.; Ghosh, D. Entropically Stabilized Compositionally Complex Prussian Blue Analogues in Electrochemical Energy Storage and Catalytic Applications. *Adv. Energy Mater.* **2026**, *16*, e05809. [CrossRef]
26. Wu, K.; Zhang, G.; Yan, B.; Pang, H. Recent Progress in Prussian Blue Analog Nanomaterials: Structural Engineering and Functional Applications. *ChemSusChem* **2026**, *19*, e202501886. [CrossRef] [PubMed]
27. Braga, M.H.; Nishchith, B.S.; Shivaramaiah, R.; Kumar, T.R. Uncovering Full-Cell Cycling Morphology Through a Rechargeable Sodium Ion Battery Based on Tungsten Oxide and Sodium Prussian Blue Intercalation Chemistry. *Battery Energy* **2026**, *5*, e70055. [CrossRef]
28. Chang, H.; Qiu, L.Y.; Chen, Y.H.; Wang, P.F.; Zhu, Y.R.; Yi, T.F. Rational construction of Prussian blue analogue with inverted pyramid morphology as ultrastable cathode material for lithium-ion battery. *Compos. B Eng.* **2023**, *250*, 110434. [CrossRef]
29. Lee, D.H.; Dhandole, L.K.; Ahn, S.H.; Mahadik, M.A.; Ryu, H.I.; Chung, H.S.; Kim, H.G.; Lim, D.H.; Jang, J.S. Controlling the ratio of Ni and Fe co-doping in a Prussian-white cathode to improve the structural stability and redox performance of advanced sodium-ion batteries. *J. Mater. Chem. A* **2026**, *14*, 3564–3573. [CrossRef]
30. Nie, C.; Zhang, X.; Ren, H.; Xing, Z.; Cao, X.; Liu, J.; Wei, D.; Ju, Z. Synthesis of Manganese-Based Prussian Blue Nanocubes with Organic Solvent as High-Performance Anodes for Lithium-Ion Batteries. *Eur. J. Inorg. Chem.* **2019**, *2019*, 3277–3286. [CrossRef]
31. Ye, W.; Yu, L.; Sun, M.; Cheng, G.; Fu, S.; Peng, S.; Han, S.; Yang, X. Yolk-shell Prussian blue analogues hierarchical microboxes: Controllably exposing active sites toward enhanced cathode performance for lithium ion batteries. *Electrochim. Acta* **2019**, *319*, 237–244. [CrossRef]
32. Zhang, X.; Yang, S.; Lu, W.; Tian, Y.; Liu, Z.; Zhao, Y.; Liu, A. One-Dimensional Co-Carbonate Hydroxide@Ni-MOFs Composite with Super Uniform Core–Shell Heterostructure for Ultrahigh Rate Performance Supercapacitor Electrode. *Small* **2022**, *18*, 2200656. [CrossRef]
33. Wu, H.; Li, S.; Liu, Y.; Mu, Q.; Shi, Y. Dual metal MOF derived Co-Ni/rGO as cathode material with synergetic effect for an asymmetric supercapacitor with enhanced performances. *J. Energy Storage* **2024**, *84*, 110864. [CrossRef]
34. Ding, Y.; Zhang, L.; Gao, X.; Wei, M.; Liu, Q.; Li, Y.; Li, Z.; Cheng, L.; Wu, M. Construction of Sugar-Gourd-Shaped Carbon Nanofibers Embedded with Heterostructured Zinc-Cobalt Selenide Nanocages for Superior Potassium-Ion Storage. *Small* **2024**, *20*, 2307095. [CrossRef]
35. Yaseen, S.; Wattoo, A.G.; Abbas, S.M.; Arfan, M.; Song, Z. Synthesis of Zn-Cu-Mn ternary metal oxide nanosheets via an integrated approach for high performance hybrid supercapacitors. *Chem. Eng. J.* **2025**, *507*, 160337. [CrossRef]

36. Guan, H.; Wei, N.; Yang, M.; Cheng, J.; He, W.; Zhang, B. Construction of $NiCo_2O_4$@CNPs core-shell nanocomposites with 2D leaf-like structure for high-performance supercapacitor. *Vacuum* **2023**, *209*, 111812. [CrossRef]
37. Hou, Z.; Wu, J.; Yan, X.; He, X.; Ivanets, A.; Bekchanov, D.; Su, X. Upcycling electroplating sludge metals into ultrathin NiFeAl-LDH nanosheets for advanced energy storage applications. *J. Energy Storage* **2025**, *128*, 117105. [CrossRef]
38. Han, R.; Pan, Y.; Yin, C.; Du, C.; Xiang, Y.; Wang, Y.; Zhu, H. Proton-self-doped PANI@CC as the cathode for high-performance aqueous zinc-ion battery. *J. Colloid Interface Sci.* **2023**, *650*, 322–329. [CrossRef]
39. Li, J.; Du, R.; Wang, R.; Feng, J.; Luo, S. Rational construction of multilayer NiCo-MOF@MnO_2 heterostructures with optimized charge storage behavior for asymmetric supercapacitors. *Appl. Surf. Sci.* **2025**, *706*, 163595. [CrossRef]
40. Qian, J.; Xu, J.; Lu, Z.; Wang, Y. Preparation of nanosphere-interspersed flower-like heterostructure of ZnS/$ZnCo_2S_4$@$Ni(OH)_2$ and its application for asymmetric solid-state supercapacitor. *J. Energy Storage* **2023**, *69*, 107945. [CrossRef]
41. Zardkhoshoui, A.M.; Mansouri, F.; Davarani, S.S.H. Hierarchical copper-nickel telluride hollow spheres embedded in reduced graphene oxide: A breakthrough in high-performance supercapacitor electrodes. *J. Energy Storage* **2025**, *132*, 117785. [CrossRef]
42. Shrivastava, A.; Smith, K.C. Electron Conduction in Nanoparticle Agglomerates Limits Apparent Na^+ Diffusion in Prussian Blue Analogue Porous Electrodes. *J. Electrochem. Soc.* **2018**, *165*, A1777. [CrossRef]

Disclaimer/Publisher's Note: The statements, opinions and data contained in all publications are solely those of the individual author(s) and contributor(s) and not of MDPI and/or the editor(s). MDPI and/or the editor(s) disclaim responsibility for any injury to people or property resulting from any ideas, methods, instructions or products referred to in the content.